MODELING OF PHASE TRANSITION IN FABRICATION OF POLYMER-DERIVED CERAMICS (PDCS)

CHI MA

Thayer School of Engineering, Dartmouth College,
Hanover, NH, 03755, U.S.A
chi.ma@dartmouth.edu

YAN LI*

Thayer School of Engineering, Dartmouth College,
Hanover, NH, 03755, U.S.A
yan.li@dartmouth.edu

Abstract

Polymer-derived ceramics (PDCs) route, which converts preceramic polymers to ceramics through heat treatment, presents a flexible and energy efficient approach to fabricate ceramic composites with arbitrary geometries and tailorable properties. Due to the huge gaps of thermal and mechanical properties of polymers and ceramics, the current state phase composition and phase distribution largely affect the heat transfer behavior and temperature field evolution that ultimately determines the subsequent polymer decomposition and phase redistribution. In this paper, a computational framework is developed to predict the continuum-level phase transition and its effect on mechanical properties. Molecular dynamics (MD) simulations are carried out first to track the atomic structure evolution and mass loss associated with gas generation. It is found that pyrolysis temperature primarily determines the amount gases that can be generated. Gas diffusion is triggered as a result of the non-uniform temperature field. Ceramic phase formation depends on the interplay between gas generation and gas diffusion. This computational framework allows real-time temperature field and phase composition map to be explicitly extracted. The phase composition map is incorporated into a finite element model for compression simulation. The effects of heating rate, pyrolysis temperature and pyrolysis time on mechanical response are systematically studied. Conclusions from this study can provide direct guidance for fabricating polymer-derived ceramics (PDCs) with tailored properties.

Keywords: Polymer-derived ceramics (PDCs); Phase transition analysis; Molecular dynamics (MD) simulation; Finite element simulation; Phase composition map.

**** Corresponding Author:*** *Yan Li (yan.li@dartmouth.edu)*

1. Introduction

Discovery of polymer-derived ceramics (PDCs) has enabled significant technological breakthroughs in ceramic science and technology. Unlike traditional ceramics processing techniques which require high temperature, high pressure and long holding times in sintering [Gonzalez *et al.*, 2018], fabrication of PDCs offers a more flexible and energy-efficient approach as this material system is made through thermal treatment of preceramic polymers at much lower temperatures without pressure [Andronenko *et al.*, 2006; Colombo *et al.*, 2010]. The polymer-to-ceramic transition opens up exciting opportunities to produce a broad spectrum of PDCs with tailored mechanical, chemical and physical properties. First of all, shaping at the polymer state can avoid problems related to tool wear and brittle fracture upon finishing the ceramic component. Currently, additive manufacturing offers a relatively inexpensive way to fabricate preceramic polymers with complex shapes and hierarchical architectures that are otherwise impossible to achieve through machining [Eckel *et al.*, 2016; Konstantinou *et al.*, 2020; Kulkarni *et al.*, 2020]. In addition to the flexibility in structure/architecture design, the phase transition process provides additional space for PDC property tailoring through careful control of key processing parameters, such as pyrolysis temperature, heating rate and holding time, etc. These capabilities will greatly extend the use of ceramics in areas, such as biomedical implants and renewable energy storage devices, where customer-specific geometry and functionality are in high demand.

Experimentally, thermogravimetric analysis (TGA) [Alvi and Akhtar, 2018; Ma *et al.*, 2018; Wilfert and Jansen, 2011] has been employed to track the mass loss associated with preceramic polymer decomposition during pyrolysis. However, this approach alone cannot resolve the atomic structure change which is important for understanding the

phase transition process. Other approaches, such as nuclear magnetic resonance (NMR) spectroscopy [Gottardo *et al.*, 2012] and X-ray computed tomography [Larson and Zok, 2018] can be combined with TGA to extract atomic rearrangements and microstructure evolution from pyrolysis intermediates. But detailed microstructure characterization has to be performed after pyrolysis through scanning electron microscopy (SEM) and/or transmission electron microscopy (TEM) [Hanniet *et al.*, 2020; Kleebe *et al.*, 1999; Toma *et al.*, 2012; Vry *et al.*, 2020]. Due to the high cost and long cycles, only limited processing routes and sample configurations can be explored experimentally. Computational models can complement experiment by extending the scope of work to arbitrary material configurations and processing parameters. Molecular dynamics (MD) models have been used to capture the atom interactions and structure change during pyrolysis. Gao *et al.* [2018] dynamically simulated the bonding topology of all atoms in preceramic polymers of hydridopolycarbosilane (HPCS) and polymethylhydrosilane (PMHS) and directly characterized the ceramic phase and gas products during pyrolysis. Their approach concerns uncrosslinked preceramic polymer with manual deletion of gas molecules during the pyrolysis simulations. Harpale *et al.* [2018] constructed a crosslinked polymer melts by applying a top free region that allows gas diffusion without molecule deletion. Although these models provide important physical aspects of atomic structure change during pyrolysis, the conclusions cannot be directly used to predict the evolution of phase composition at the structure level. Bernard *et al.* [2006] developed a diffusion-controlled kinetic model to predict phase transition in poly[B-(methylamino)borazine] precursors. However, temperature evolution and its effect on phase interactions and phase composition map were not considered. In fact, temperature evolution and phase transition are interconnected in this highly dynamic event. First, temperature determines the initiation of polymer decomposition and gas generation. The region which has been converted to ceramics exhibits much higher thermal conductivity than that in the polymer phase and intermediate phase. Therefore, quantification of current state phase composition is essential for predicting the temperature redistribution and subsequent phase transition. The intricate coupling between heat transfer and phase transition has not been systematically established yet.

The computational framework presented in this paper innovatively predicts continuum-scale ceramic phase formation by elucidating the interplay between gas generation and gas diffusion. Molecular dynamics (MD) simulations are carried out first in Section 2 to capture the gas generation during pyrolysis. Coupled heat transfer and phase transition analysis are discussed in Section 3. This computational framework provides detailed spatial and temporal resolutions (e.g., real-time temperature field and phase composition map) that experiment alone cannot resolve. The phase composition map, which is transferred to the compression simulation, can be explicitly extracted at any stage of pyrolysis. The effect of processing parameters on phase composition evolution are systematically studied. The overall flowchart of the computational framework is shown in Fig. 1. Computations in this paper concern polymethylhydrosiloxane (PMHS) crosslinked by divinylbenzene (DVB). But the approach itself can be applied to other PDCs systems. The failure and deformation mechanisms in PMHS/DVB samples and their correlation with heating rate and pyrolysis temperature are discussed in Section 4.

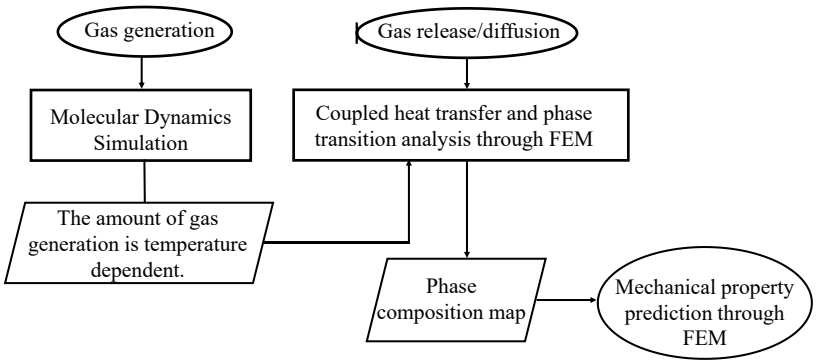

Fig. 1 Flowchart of computational framework.

2. Molecular dynamics (MD) simulation of crosslinking and pyrolysis

A MD model is developed to simulate the chemical reaction and atomic structure change during the polymer-to-ceramic phase transition. Calculations concern both crosslinking and pyrolysis processes. Cross-linking is the first treatment which preceramic polymer undergoes after being shaped. The purpose is to form chemical bonds among polymer chains and create a network to constrain chains' motion [Ji *et al.*, 2018; Ma *et al.*, 2017]. In this study, an equilibrated system of PMHS with DVB is built in Materials Studio using all-atom polymer consistent force field (PCFF). The repeating units are illustrated in Fig. 2(a). As shown in Fig. 2(b), one PMHS molecule is constructed by 25 repeating units and pre-crosslinked with 6 DVB molecules following the hydrosilylation process [Taheri *et al.*, 2020]. This configuration is selected by considering the average molecular weight of PMHS as 1500 g/mol and the molar mass of one PMHS repeat unit as 60 g/mol, respectively. During the cross-linking process, a C-C double bond in DVB is opened first. The atom H, which is initially connected to Si in a PMHS molecule, is replaced by a C atom at the end of a DVB molecule. The formation of Si-C bond between the PMHS and DVB leads to partially crosslinked chains that are packed to the target density of 1.0 g/cc, as illustrated in Fig. 2(c).

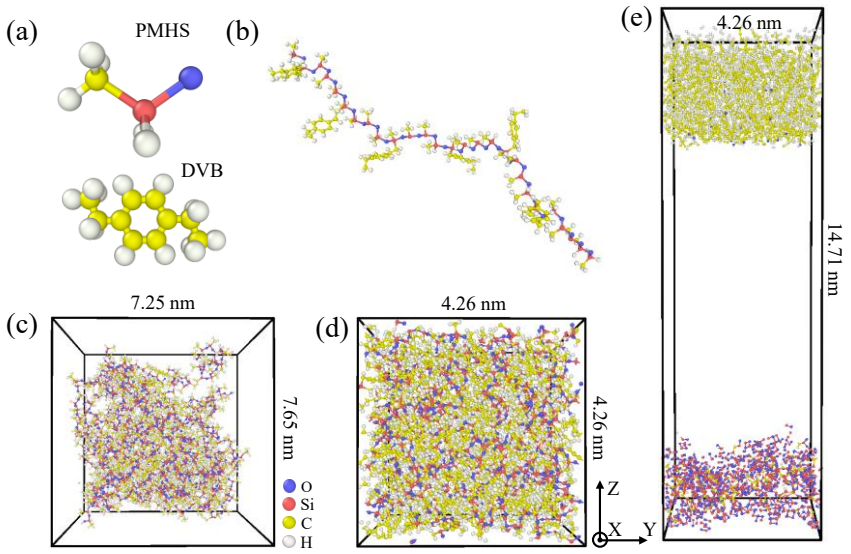

Fig. 2 (a) PMHS and DVB monomers; (b) Partially pre-crosslinked PMHS/DVB molecules; (c) Initial atomic configuration; (d) Equilibrated fully-crosslinked PMHS/DVB mixture; and (e) System configuration after pyrolysis.

The atomic configuration of the packed PMHS/DVB mixture (Fig. 2(c)) and charge on each atom are imported into large-scale atomic/molecular massively parallel simulator (LAMMPS) [Plimpton, 1995] for further equilibrium. The choice of reaction force fields for achieving system equilibrium follows the work of Kulkarni *et al.* [2013], where the interaction parameters of Si, O, C and H elements are provided. In this work, constant temperature and constant pressure ensemble (NPT) are applied to the simulation box with periodic boundary conditions in all directions. This equilibrium step takes 40 ps with a time step of 0.1 fs under the temperature of 400 K. Once the system equilibrium is reached, the temperature is gradually reduced to the room temperature of 300 K within 5 ps. Based on the bonding length, new chemical bonds are created between the unbonded end of DVB and Si atoms in PMHS. The equilibrated system with the box length of 4.26 nm in Fig. 2(d) is employed for the pyrolysis step.

A systematic set of pyrolysis simulations is conducted by heating up the equilibrated system to a range of final temperatures (1500 K to 2500 K) with a heating rate of 0.1 K/fs and a time step of 0.2 fs. During the course of pyrolysis, gases, such as hydrogen, methane and other carbon- and hydrogen-contained species will be generated due to bond breaking (e.g. Si-H, Si-CH_3) and new bond formation (e.g. H-H, CH_3-H). Some of the existing work [Gao *et al.*, 2018; Ponomarev *et al.*, 2019] considers the algorithm that deletes the gas molecules every few picoseconds. In

this work, another approach is adopted to capture the gas generation activities during pyrolysis. Here, the top surface of the simulation box is set to move freely along the vertical direction. At the height of three times of the initial box length, the temperature is set to 0.1 K by Berendsen thermostat in order to trap the gas molecules. The periodic boundary conditions are applied to the other two directions. The time step used in pyrolysis is 0.2 fs and temperature of all regions is controlled by Berendsen thermostat. Mass loss percentage is counted as the ratio between the total mass of generated gaseous molecules that are trapped at the top (Fig. 2(e)) as well as the initial system mass. According to Fig. 3(a), a saturation plateau of mass loss percentage is observed at different pyrolysis temperature. The mass loss rate r, which is calculated as the slope of the linear region in Fig. 3(a), is fitted as a function of the reciprocal of temperature. As shown in Fig. 3(b), r almost linearly varies with $1/T$. It can be referred from the linear relationship that the mass loss rate at 873 K is approximately 1.46×10^{-3} %/ps. This indicates that the time required for complete gas generation is only 68 ns. A shorter time is needed when the pyrolysis temperature increases. Therefore, it is reasonable to consider instant gas generation at the structure scale when the pyrolysis temperature reaches the threshold for polymer decomposition. The total amount of gaseous products that can be generated only depends on the pyrolysis temperature. This conclusion is used to formulate the structure-level ceramic fraction as discussed in Section 3.

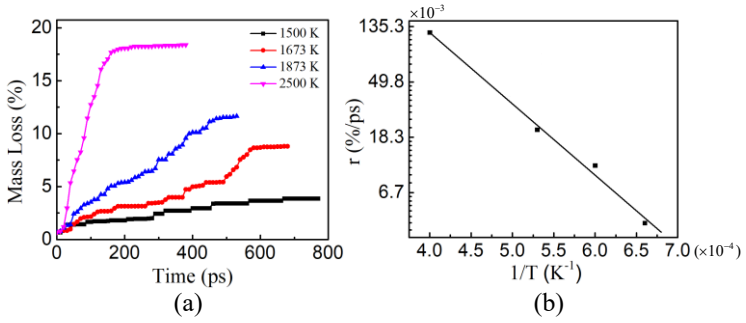

Fig. 3 (a). Evolution of mass loss percentage at different pyrolysis temperature T and (b). Fitted mass loss rate with respect to 1/T.

3. Coupled heat transfer and phase transition analysis

Ceramic structure formation is the process of bond reformation, which occurs locally due to the low self-diffusion coefficient of solid phase. This process requires the gaseous molecules which are generated during polymer decomposition to diffuse out of the system so that the new ceramic structure can be formed [Bernard *et al.*, 2006]. As discussed in Section 2, the total amount of gases that can be generated at time t primarily depends on the current pyrolysis temperature T. During the course of pyrolysis, there are three possible phases in the sample: 1). polymer phase (phase 1), ceramic phase (phase 2), and intermediate phase (phase 3) with partially decomposed polymers. Due to the huge discrepancy of thermal conductivity in each phase, temperature distribution inside the sample is non-uniform, especially at the early stage of pyrolysis. Therefore, various amounts of gases will be generated at different spatial locations. Gas diffusion is triggered as a result of gas density gradient. As the polymer phase is gradually converted to the ceramic phase, heat transfer in the sample is promoted. This is because the thermal conductivity of ceramics is about ten times higher than that of polymers [Stabler *et al.*, 2018]. It can be concluded that the current state material phase composition and phase distribution significantly affect the heat transfer behavior and in turn the temperature field distribution which determines the subsequent polymer decomposition and phase redistribution. However, important information, such as real-time temperature field and phase composition map, cannot be directly extracted from the existing experimentation. The computational model developed here can bridge the knowledge gap by linking atomic information to continuum-level heat transfer and phase transition analysis.

3.1 Prediction of continuum-level phase transition

Ceramic phase formation at the continuum level depends on the interplay between gas generation and gas diffusion. The generated gas density $\psi(T)$ is calculated according to

$$\psi(T) = m_{gas}(T)\rho_{\text{initial}} / m_{\text{initial}} = m_{loss}(T)\rho_{\text{initial}}, \tag{1}$$

where $m_{gas}(T)$ is the mass of generated gas products at temperature T. m_{initial} is the initial system mass. $\rho_{\text{initial}} = 1.21$ g/cc is calculated from the atomic structure as shown in Fig. 2(d). $m_{loss}(T)$ is the mass loss ratio. Experimentally, $m_{loss}(T)$ is extracted through thermogravimetric (TGA) analysis [Li *et al.*, 2018]. According to Fig. 3(a), gas generation can complete within a few tens of nanoseconds. During this very short time period, it is reasonable to assume uniform distribution of gas molecules in this system [Gao *et al.*, 2018]. Therefore, the gas volume in eqn. (1) is considered the same as the total system volume during this instant gas generation process. The gas diffusion rate $\partial\psi / \partial t$ is calculated based on the current gas density as

$$\frac{\partial \psi}{\partial t} = D_{\text{T}} \nabla^2 \psi(x, y, z, t). \tag{2}$$

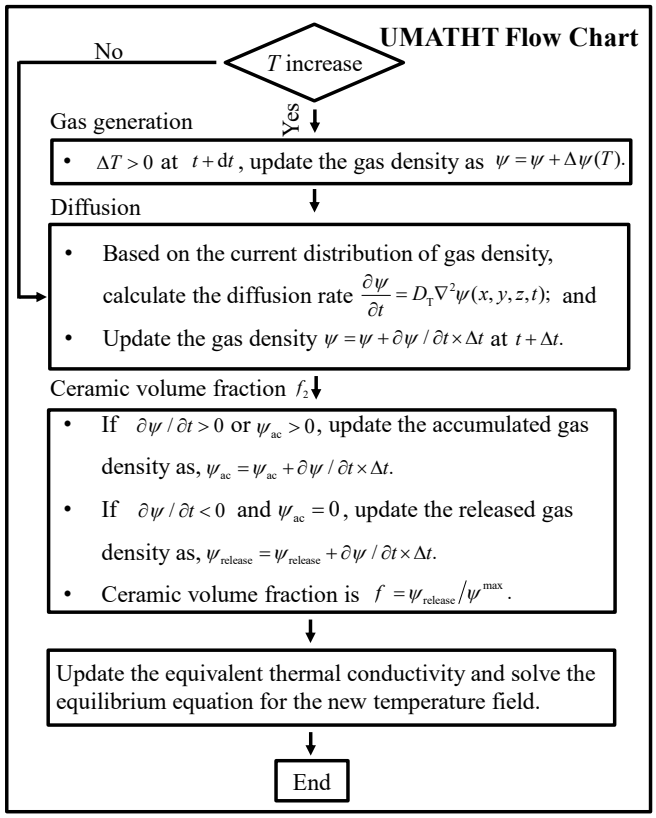

ψ	-	Gas density
D_{T}	-	Diffusion coefficients
ψ_{ac}	-	Density of the accumulated gas
ψ_{release}	-	Density of the released gas
ψ^{max}	-	Maximum gas density that can be generated in a given element

Fig. 4 Algorithm for calculating the ceramic phase transition based on temperature evolution and gas diffusion kinetics.

Here D_T is the diffusion coefficient estimated according to Merkel et. al [Merkel *et al.*, 2000]. Phase transition requires the generated gaseous products to release out of the system so that the ceramic structure can be formed. At an arbitrary element, this scenario corresponds to $\partial\psi / \partial t < 0$. The ceramic fraction f is predicted as

$$f = \frac{\psi_{\text{release}}}{\psi^{\max}}, \tag{3}$$

where ψ_{release} and $\psi^{\max}$ are the released gas density and maximum gas density that can be generated in a given element. The formulation in eqn. (3) assumes that the volume of each element is unchanged during the phase transition process. Therefore, the gas density is essentially the mass loss which is used to quantify the ceramic yield experimentally [Ma *et al.*, 2018]. The detailed algorithm, which calculates the phase transition by considering temperature evolution and gas diffusion kinetics, is developed through a user subroutine UMATHT in ABAQUS as illustrated in Fig. 4. The effect of temperature on gas generation, gas diffusion and ceramic formation is discussed in Section 3.3.

3.2 Thermal property evaluation in the intermediate zone

The equivalent thermal conductivity k_3 in the intermediate zone is calculated according to the Mori-Tanaka method as [Benveniste, 1986; Böhm and Nogales, 2008]

$$k_3 = \frac{2k_1^2 + k_1k_2 - 2fk_1(k_1 - k_2)}{2k_1 + k_2 + f(k_1 - k_2)}. \tag{4}$$

Here, f is the ceramic fraction in the intermediate phase according to eqn. (3). k_1 and k_2 represent the thermal conductivity of the polymer phase and ceramic phase, respectively. The equivalent specific heat capacity and density in the intermediate phase are calculated as,

$$c_3 = (1-f)c_1 + fc_2, \text{ and} \tag{5}$$

$$\rho_3 = (1-f)\rho_1 + f\rho_2. \tag{6}$$

Here, c_1, c_2 and ρ_1, ρ_2 are specific heat capacity and density of the polymer phase and ceramic phase, respectively. The thermal properties of these two phases are summarized in Table 1. The current temperature field in the system is obtained by solving the thermal energy equilibrium as

$$\int_V \rho_i c_i \frac{\partial T}{\partial t} \mathrm{d}V = \int_V k_i \left(\frac{\partial^2 T}{\partial x^2} + \frac{\partial^2 T}{\partial y^2} + \frac{\partial^2 T}{\partial z^2}\right) \mathrm{d}V, \tag{7}$$

where $i = 1, 2, 3$ represent polymer phase, ceramic phase and intermediate phase, respectively. k_3 is updated in each time step in response to the phase composition change. Latent heat is not considered in the current work.

Table 1. Summary of thermal properties in PMHS and amorphous ceramics SiOC.

Materials	Density ρ ($\mathrm{g \cdot cm^{-3}}$)	Specific heat capacity c ($\mathrm{J \cdot K^{-1} \cdot g^{-1}}$)	Thermal conductivity k ($\mathrm{W \cdot K^{-1} \cdot m^{-1}}$)
PMHS (Phase 1)	1.21	1.43 [Smirnova *et al.*, 2007]	0.15 [Zhang *et al.*, 2020]
Amorphous SiOC (Phase 2)	1.75 [Lu *et al.*, 2016]	1.1 [Stabler *et al.*, 2018]	1.5 [Stabler *et al.*, 2018]

3.3 Correlation between phase transition and gas diffusion kinetics

A cubic sample with side dimension of 20 mm is constructed as shown in Fig. 5(a). The pyrolysis history is characterized by the heating rate, pyrolysis temperature and holding time as illustrated in Fig. 5(b). Fig. 6 illustrates the phase transition process at a pyrolysis temperature of 1273 K and heating rate of 0.63 K/s. The temperature field and phase composition map are captured at 500 s, 1000 s and 1600 s, respectively. It is noted that higher temperature gradient is observed at the initial pyrolysis stage where the applied surface temperature linearly increases with time. As shown in Fig. 6, temperature at the center of the sample is approximately half of that at the surface when the pyrolysis is conducted for 500 s. As the pyrolysis proceeds, the temperature gradient gradually decreases with time. At the time of 1600 s, a homogenous temperature field of 1273 K is observed.

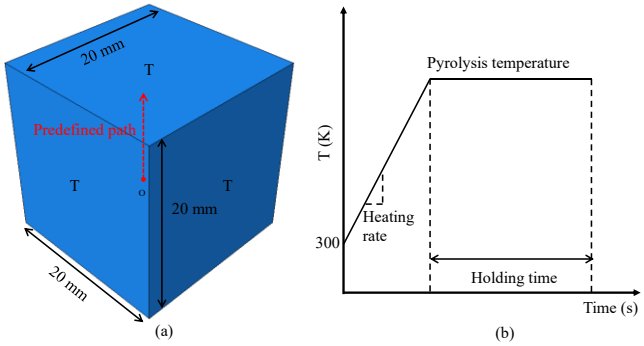

Fig. 5 (a) Scheme of model configuration with controlled surface temperature and (b) applied surface heating history.

Based on the given heating condition, polymer decomposition initiates from the outer surface and gradually propagates to the inner part of the sample. At 500 s, polymer decomposition has occurred at the outer surface but has not reached to the inner region where the average temperature is around 450 K. At 1600 s, only a thin layer of fully converted ceramics is observed near the outer surface even though the entire temperature field has reached the uniform state of 1273 K. In fact, it takes 2440 s to fully complete the ceramization process based on the given heating history. It can be inferred that polymer decomposition lags behind the temperature rise. In order to illustrate this point, both the temperature and ceramic formation data are extracted along the predefined path which starts from the center of the cube and ends at a point with distance of 9 mm as illustrated in Fig. 5(a). It can be seen from Fig. 7(a) that temperature near the outer layer (distance = 9 mm) is 1.4 times that at the center (distance = 0 mm) when the sample is being pyrolyzed for 80 s. Polymer decomposition only exist in regions where the distance from the sample center is greater than 7 mm. During the course of pyrolysis, the sample composition gradually changed from pure polymer phase to ceramic phase dominated composite as indicated in Fig. 7(b). The corresponding temperature gradient from the center to the outer surface also diminishes. This is expected as the ceramic phase formation promotes the heat transfer and in turn accelerates the subsequent polymer decomposition.

This conclusion can be further explained through the gas activity analysis in Fig. 8. As shown in Fig. 8(a), the gas density at 80 s and 160 s exhibits a peak value in the vicinity of the sample surface. Therefore, gas diffusion in this region can follow two directions as illustrated in Fig. 8(b). At a given time, an element can receive newly generated gases as a result of polymer decomposition. If the gas density in this element is lower than that in the adjacent places, additional gases can diffuse into this element, causing gas accumulation. Reversely, gas release takes place. The competition between gas accumulation and gas release at 160 s is illustrated in Fig. 8(b). It is noted that gas accumulation is the dominant mechanism when the distance from the sample center is below 6 mm. Beyond this point, gas release takes the dominance and quickly increases as the sample surface is approached. As the ceramic phase starts to emerge at the outer surface, the overall thermal conductivity of the sample increases accordingly. The enhanced heat transfer intensifies the subsequent polymer decomposition. The location where the maximum gas density is

reached gradually shifts to the inner part of the sample due to the diminishing gas release. As shown in Fig. 8(c), the maximum gas density is reached at the center at 1000 s. Only one gas flow path is observed due to the redistributed gas density gradient.

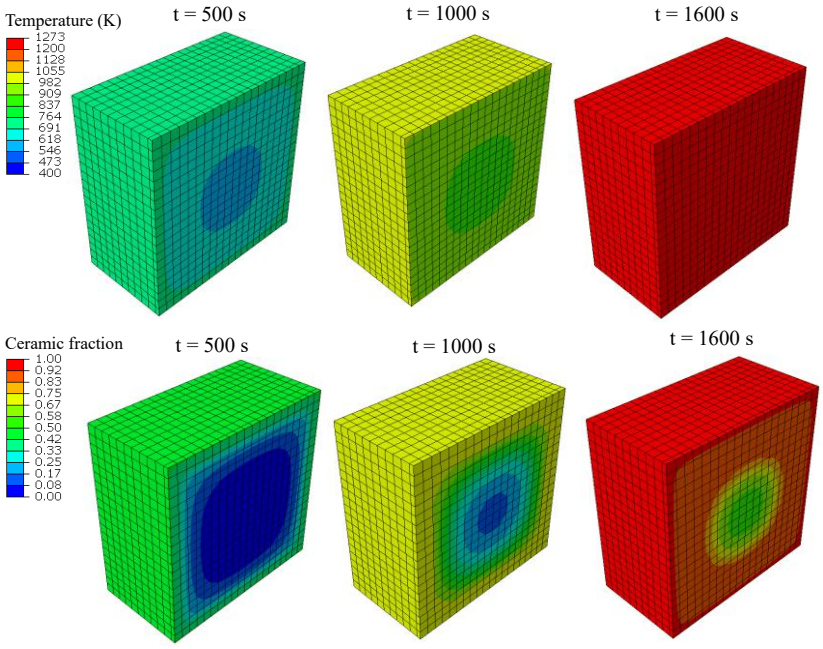

Fig. 6 Evolution of temperature and phase composition under the pyrolysis temperature of 1273 K and heating rate of 0.63 K/s.

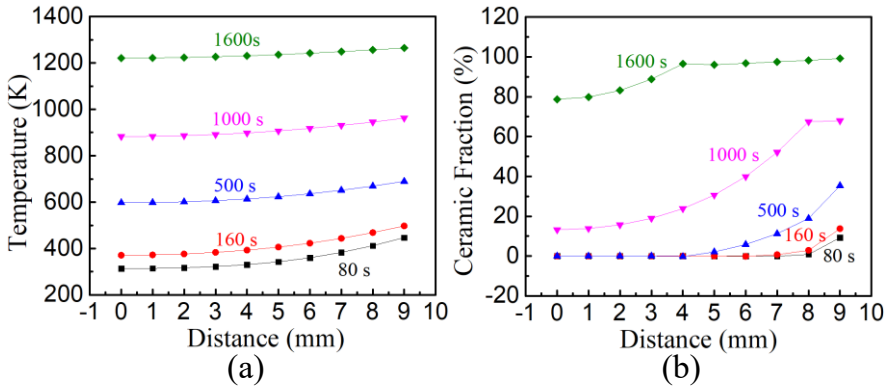

Fig. 7 Spatial distribution of (a) temperature and (b) ceramic fraction at different times under pyrolysis temperature of 1273 K and heating rate of 0.63 K/s.

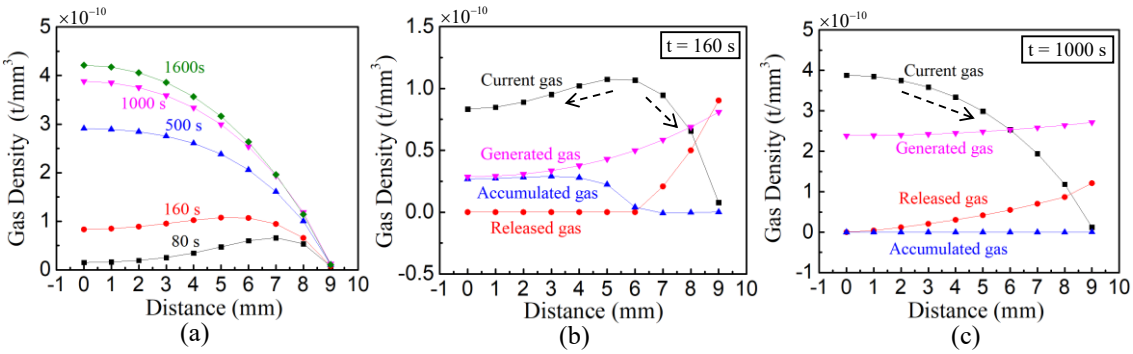

Fig. 8 (a) Spatial distribution of current gas density at different times; Spatial distribution of current gas, released gas, accumulated gas, and generated gas at (b) 160 s and (c) 1000 s, respectively.

4. Mechanical property prediction

Phase transition analysis in Section 3 allows the phase composition map to be directly extracted from an arbitrary sample configuration with predefined heating history. A few sets of phase composition maps are generated based on systematically varied heating rates, pyrolysis temperature and pyrolysis time. Each phase composition map is incorporated into a finite element model as shown in Fig. 9 for compression simulation. To simplify the calculation, we decompose the pyrolyzed sample domain in seven regions based on the calculated ceramic fraction f. The region arrangements are listed in Table 2. Fig. 9(a) illustrates the domain decomposition of a cubic sample which is pyrolyzed at 1273 K for 1200 s under the heating rate of 0.63 K/s. A boundary velocity of $v = 0.2$ mm/s is imposed at the top surface of the sample, while the bottom surface is fixed. The constitutive relationship in Region P (pure polymer region) follows the experiment data from Kim et. al [Kim *et al.*, 2011]. Material in region C (pure ceramic region) follows the isotropic linear elastic constitutive relation with Young's modulus $E_c = 101$ GPa and poisson's ratio $\nu_c = 0.11$. The constitutive behaviors in region 2 to region 5 are determined through the 1/8 symmetric compression simulations as shown in Fig. 9(b). It is assumed that damage would occur when the equivalent stress reaches $\sigma^{\mathrm{P}}_{\mathrm{eq\_max}} = 1.5$ MPa in region P [Kim *et al.*, 2011] and $\sigma^{\mathrm{C}}_{\mathrm{eq\_max}} = 200$ MPa in region C [Vozza, 2021], respectively. This critical stress in region 2 to region 5 is determined through

$$\sigma^{i}_{\mathrm{eq\_max}} = f^{i}_{ave} \times \sigma^{\mathrm{C}}_{\mathrm{eq\_max}} + (1 - f^{i}_{ave}) \times \sigma^{\mathrm{P}}_{\mathrm{eq\_max}}, \tag{8}$$

where $\sigma^{i}_{\mathrm{eq\_max}}$ is the maximum equivalent stress of region i, and f^{i}_{ave} is the averaged ceramic fraction in region i when $2 \le i \le 5$. Due to the lack of experiment data in the existing literature, simplified constitutive relations are considered in this initial study. But more involved constitutive models will be developed in our future work.

Table 2. Criterion for sample domain decomposition.

Different regions	Ceramic fraction
Region P	f=0
Region 1	$0 < f \le 20\%$
Region 2	$20\% < f \le 40\%$
Region 3	$40\% < f \le 60\%$
Region 4	$60\% < f \le 80\%$
Region 5	$80\% < f < 100\%$
Region C	f=100%

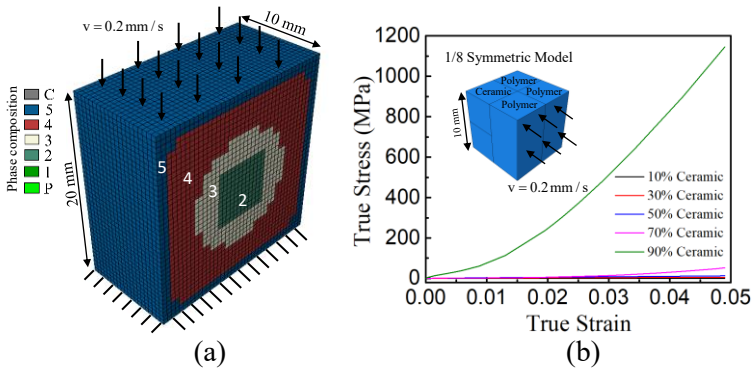

Fig. 9(a) Scheme of sample configuration with domain decomposition in the middle surface; and (b) Constitutive behaviors in the selected domains.

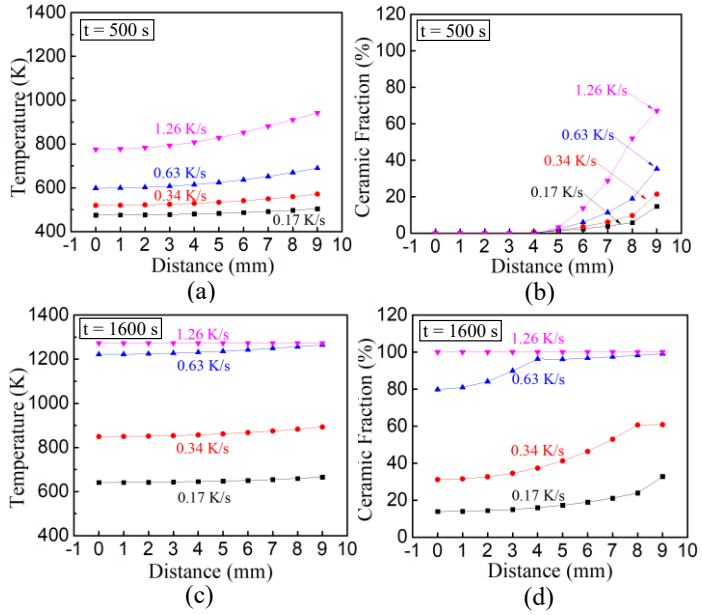

Fig. 10 Effect of heating rate on (a) temperature distribution and (b) ceramic fraction at 500 s; Effect of heating rate on (c) temperature distribution and (d) ceramic fraction at 1600 s.

5. Results and discussion

5.1 Effect of heating rate on phase transition

In this set of calculations, the pyrolysis temperature is kept as 1273 K while the heating rate of 0.17 K/s, 0.34 K/s, 0.63 K/s and 1.26 K/s is applied to the sample in Fig. 5, respectively. The effect of heating rate on temperature distribution and ceramic phase formation is summarized in Fig. 10. It is found that heating rate plays a more important role at the initial stage of pyrolysis. As shown in Fig. 10(a), the temperature gradient between the sample center and the outer surface is only 29 K at 500 s when the heating rate is 0.17 K/s. This gradient increases to 167 K when the heating rate is raised to 1.26 K/s. As indicated in Fig. 10(b), heating rate has a negligible effect on ceramic formation in the inner part of the sample where the distance to the center is below 4 mm. This again proves that ceramization requires gas diffusion which lags behind gas generation. When the pyrolysis time reaches 1600 s, the temperature

distribution in each case tends to be uniform regardless of the heating rate (Fig. 10(c)). At the highest heating rate of 1.26 K/s, the entire sample has been fully converted to the ceramic phase according to Fig. 10(d). When the heating rate decreases to 0.63 K/s, only the outer surface of the sample has reached the ceramic state. A plateau of ceramic fraction is observed even though there is no obvious temperature change at this transition. This is because a higher amount of accumulated gas in the inner region leads to slower ceramization compared to the that occurs at the outer surface.

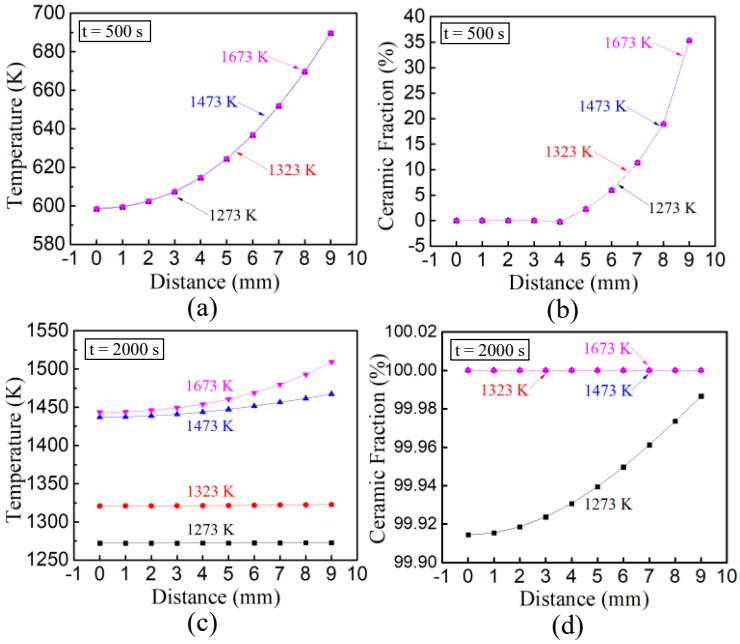

Fig. 11 Effect of pyrolysis temperature on (a) temperature field distribution and (b) ceramic formation at 500 s; Effect of pyrolysis temperature on (a) temperature field distribution and (b) ceramic formation at 2000 s.

5.2 Effect of pyrolysis temperature on phase transition

In this set of calculations, heating rate is kept at 0.63 K/s. According to the heating history in Fig. 5(b), pyrolysis temperature of 1273 K, 1323 K, 1473 K and 1673 K is reached at 1587 s, 1667 s, 1905 s and 2222 s, respectively. At the time of 500 s, no case has reached the temperature plateau yet. Due to the constant heating rate, the temperature field in all the samples build up in the same way as shown in Fig. 11(a). This leads to identical ceramic phase formation according to Fig. 11(b). At the time of 2000 s, the pyrolysis temperature beyond 1273 K only affects the temperature field distribution, but not the ceramic phase formation (Fig. 11(d)). This conclusion is consistent with the TGA analysis as the mass loss and ceramic yield remain unchanged once the temperature exceeds a certain threshold [Ma *et al.*, 2018]. Further temperature increase will only affect the ceramic structure change from amorphous state to crystalline state.

5.3 Effect of heating rate, pyrolysis temperature and pyrolysis time on mechanical response

According to the phase analysis in Section 5.1 and 5.2, heating rate, pyrolysis time and pyrolysis temperature combine to affect the phase composition and distribution. To illustrate the effect of heating rate on compressive response of the pyrolyzed samples, we first keep the pyrolysis temperature at 1273 K and extract the phase composition map at 1200 s with the heating rate of 0.17 K/s, 0.63 K/s and 1.26 K/s, respectively. The corresponding engineering stress-strain relations are summarized in Fig. 12 according to the compression simulation in Fig. 9. It is noticed that the stress-strain response at 0.17 K/s approximates the ductile behavior in region P (pure polymer phase). Due to the partial polymer decomposition, the material exhibits higher strength but lower ductility than the pure polymer phase. When

the heating rate increases to 1.26 K/s, the material behaves in a brittle manner like the pure ceramic phase in region C. If a heating rate of 0.63 K/s is applied, the stress drops abruptly at the strain of 0.02. This is due to the crack initiation at the interface between region 4 and region 5 as shown in Fig. 13. The cracks propagate towards the outer surface where a higher ceramic fraction f is predicted. It is noted that these cracks are gradually closed under further compression. No additional cracks propatate into the inner part of the material or propagate along the interface. This mechanism allows the sample to continue carrying load without immediate fracture. When a heating rate of 1.26 K/s is applied, the majority of the sample has been converted to ceramics. As shown in Fig. 14, the interface between phase C and phase 5 cannot effectively impede crack propagation. The material no longer has the ability to regain strength after the abrupt unloading.

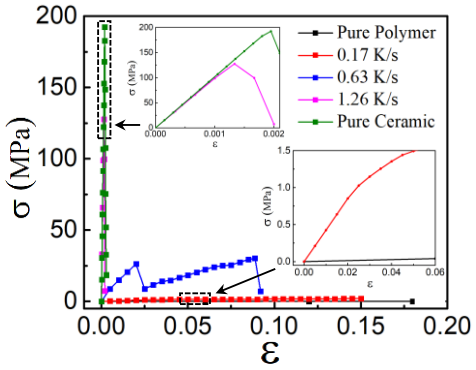

Fig. 12 Effect of heating rate on compressive response of PMHS/DVB samples being pyrolyzed at 1273 K for 1200 s.

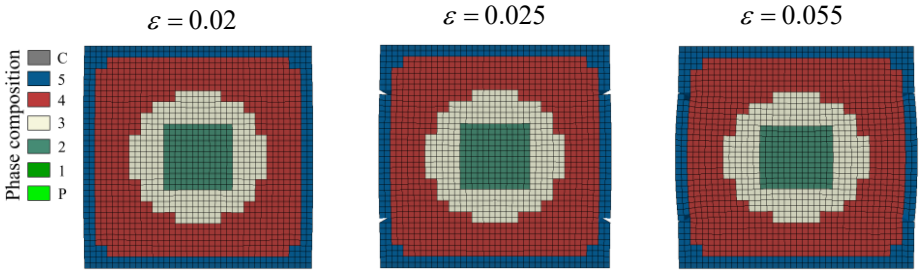

Fig. 13 Damage evolution during compression in a pyrolyzed sample with heating rate of 0.63 K/s, pyrolysis temperature of 1273 K and pyrolysis time of 1200 s.

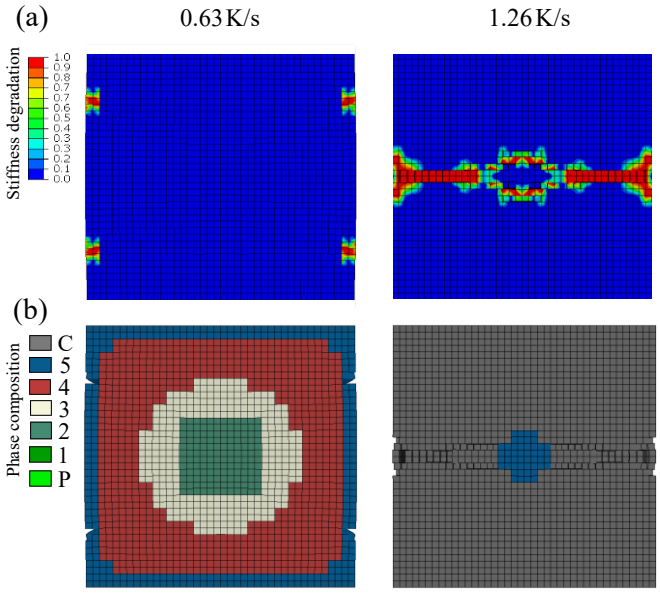

Fig. 14 (a). Damage distribution and (b) phase composition map at the heating rate of 0.63 K/s and 1.26 K/s, respectively. The pyrolysis temperature is 1273 K with duration of 1200 s.

Under the constant pyrolysis temperature of 1273 K and heating rate of 0.63 K/s, samples are pyrolyzed for 1200 s, 1360 s, 1540 s and 1700 s, respectively. According to the predicted stress-strain curves in Fig. 15(a), samples being pyrolyzed for 1200 s and 1360 s can regain strength after the initial stress drop. As indicated in Fig. 15(b), the interface between phase 4 and phase 5 can effectively arrest the existing cracks from propagation. No other cracks are observed at other interfaces. The material response becomes brittle when the pyrolysis time is longer than 1540 s. It should be noted that the pyrolyzed sample exhibit higher strength but lower ductility than the pure polymer phase when the pyrolysis time extends from 1200 s to 1360 s. This is expected as material strength and ductility are usually exclusive. However, when the pyrolysis time is between 1540 s and 1700 s, the increase of material strength from 51 MPa to 146 MPa is associated with slightly improved ductility. As shown in Fig. 15(b), crack coalescence throughout the cross-section plane at 1540 s leads to compromised material strength.

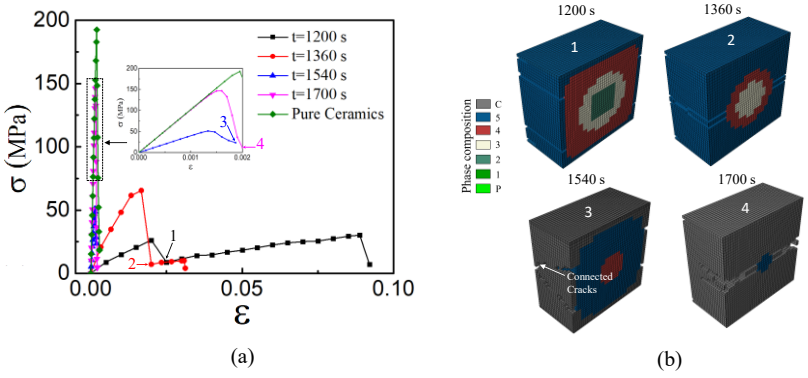

Fig. 15 (a). Stress-strain response and (b) damage illustration in samples under different pyrolysis durations. Constant pyrolysis temperature of 1273 K and heating rate of 0.63 K/s are applied.

A similar trend is observed when the pyrolysis temperature increases from 1273 K to 1673 K under the same heating rate of 0.63 K/s. As shown in Fig. 16(a), the material strength is improved without scarifying the ductility when the

pyrolysis temperature increases from 1273 K to 1473 K. Further increase of pyrolysis temperature to 1673 K leads to slightly improved ductility but negligible strength enhancement. It should be noted that the strength and ductility in a pure ceramic sample are higher than cases with intermediate phases in Fig. 16(a). This indicates that the residual intermediate phase is detrimental for both material strength and ductility if majority of the sample has been fully converted to ceramics. As shown in Fig. 16(b), lower pyrolysis temperature leads to larger intermediate region which results in more intensive damages.

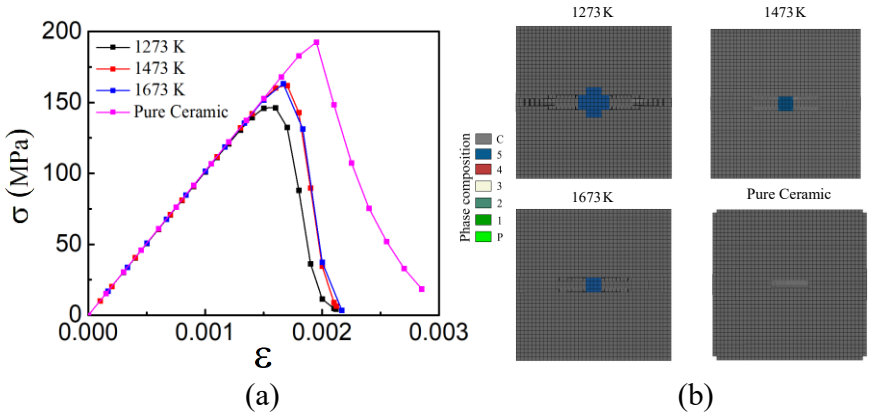

Fig. 16 (a). Stress-strain response and (b) damage illustration in samples under different pyrolysis temperature. Constant pyrolysis duration of 1700 s and heating rate of 0.63 K/s are applied.

It can be concluded from the above analyses that both material strength and ductility can be improved if the sample can regain strength after initial stress drop. However, this mechanism does not exist in cases where the majority of sample has been fully converted to ceramics. The computational framework developed here allows effective property tailoring of PDC composites through careful selection of heating rate, pyrolysis temperature and time. As an initial study, the calculations carried out here do not consider the evolution of pores, which is an inevitable outcome due to gas release if no fillers are added to the preceramic resin. It has been reported that incorporation of fillers, either active or passive, into the preceramic polymers can alleviate the pore formation [Colombo *et al.*, 2010]. However, the property mismatch between the filler and the preceramic polymer can possibility create new weak links along the interface. The interface property evaluation becomes even more complex during the pyrolysis when the preceramic polymer matrix is experiencing dynamic phase transition. A more involved model, which accounts for the interaction and/or chemical reactions between the filler and the dynamically changed matrix, will provide more realistic predictions of material properties. This would be an interesting topic for future studies.

6. Summary

A computational framework is developed to understand the dynamic phase transition process in PMHS/DVB. MD simulations are carried out first to capture the atomic structure changes during pyrolysis. The MD results indicate that gas generation at the structure scale occurs instantly when the pyrolysis temperature reaches the threshold for polymer decomposition. Gas diffusion is triggered as a result of spatial gas density gradient due to the non-uniform temperature and phase distribution. Ceramic phase formation is predicted by accounting for the interplay between gas generation and gas diffusion. The phase composition map, which is extracted through the coupled heat transfer and phase transition analysis, is incorporated in a finite element model for mechanical property evaluation. It is found that heating rate, pyrolysis temperature and pyrolysis time combine to affect the mechanical response of the pyrolyzed sample. Certain phase composition maps can lead to improved material strength without sacrificing the ductility. Although calculations in this work only consider PMHS/DVB, the developed approaches can be applied to other PDC systems.

Extension of this work will allow phase composition map to be predicted in any PDC sample configurations under arbitrary heating/cooling histories. This information is crucial in determining the material mechanical/electrical properties as function of structure architecture and processing parameters. Conclusions from this work can serve as a roadmap for fabricating PDCs with tailored properties. Additionally, future work will also address the role of pore defects on material properties due to the gas release.

7. Acknowledgement

The authors acknowledge the support from NH BioMade Project which is provided by the National Science Foundation's Research Infrastructure Improvement Award # 1757371, as well as the start-up funds from Thayer School of Engineering at Dartmouth College.

8. References

Alvi, S.A., Akhtar, F., [2018] "High temperature tribology of polymer derived ceramic composite coatings," Scientific Reports 8, 15105.

Andronenko, S.I., Stiharu, I., Misra, S.K., [2006] "Synthesis and characterization of polyureasilazane derived SiCN ceramics," Journal of applied physics 99, 113907.

Benveniste, Y., [1986] "On the effective thermal conductivity of multiphase composites," Zeitschrift für angewandte Mathematik und Physik ZAMP 37, 696-713.

Bernard, S., Fiaty, K., Cornu, D., Miele, P., Laurent, P., [2006] "Kinetic modeling of the polymer-derived ceramics route: investigation of the thermal decomposition kinetics of poly [B-(methylamino) borazine] precursors into boron nitride," The Journal of Physical Chemistry B 110, 9048-9060.

Böhm, H.J., Nogales, S., [2008] "Mori-Tanaka models for the thermal conductivity of composites with interfacial resistance and particle size distributions," Composites Science and Technology 68, 1181-1187.

Colombo, P., Mera, G., Riedel, R., Sorarù, G.D., [2010] "Polymer-derived ceramics: 40 Years of research and innovation in advanced ceramics," Journal of the American Ceramic Society 93, 1805-1837.

Eckel, Z.C., Zhou, C., Martin, J.H., Jacobsen, A.J., Carter, W.B., Schaedler, T.A., [2016] "Additive manufacturing of polymer-derived ceramics," Science 351, 58-62.

Gao, H., Wang, H., Zhao, Z., Niu, M., Su, L., Wei, Y., [2018] "Reactive dynamics simulation study on the pyrolysis of polymer precursors to generate amorphous silicon oxycarbide structures," The Journal of Physical Chemistry C 122, 5767-5773.

Gonzalez, J., Cano, S., Schuschnigg, S., Kukla, C., Sapkota, J., Holzer, C., [2018] "Additive manufacturing of metallic and ceramic components by the material extrusion of highly-filled polymers: A review and future perspectives," Materials 11, 840.

Gottardo, L., Bernard, S., Gervais, C., Weinmann, M., Miele, P., [2012] "Study of the intermediate pyrolysis steps and mechanism identification of polymer-derived SiBCN ceramics," Journal of Materials Chemistry 22, 17923-17933.

Hanniet, Q., Boussmen, M., Barés, J., Huon, V., Iatsunskyi, I., Coy, E., Bechelany, M., Gervais, C., Voiry, D., Miele, P., Salameh, C., [2020] "Investigation of polymer-derived Si–(B)–C–N ceramic/reduced graphene oxide composite systems as active catalysts towards the hydrogen evolution reaction," Scientific Reports 10, 22003.

Harpale, A., Sawant, S., Kumar, R., Levin, D., Chew, H.B., [2018] "Ablative thermal protection systems: Pyrolysis modeling by scale-bridging molecular dynamics," Carbon 130, 315-324.

Ji, T., Ma, C., Brisbin, L., Dong, Y., Zhu, J., [2018] "Effect of interface on the mechanical behavior of polybutadiene–silica composites: an experimental and simulation study," Journal of Applied Polymer Science 135, 46089.

Kim, T.K., Kim, J.K., Jeong, O.C., [2011] "Measurement of nonlinear mechanical properties of PDMS elastomer," Microelectronic Engineering 88, 1982-1985.

Kleebe, H.J., Suttor, D., Ziegler, G., [1999] "Microstructure Evolution and Crystallization Behavior of Polymer-Derived Si-C-N Monoliths: A TEM Study," Precursor-Derived Ceramics, pp. 113-131.

Konstantinou, G., Kakkava, E., Hagelüken, L., Sasikumar, P.V.W., Wang, J., Makowska, M.G., Blugan, G., Nianias, N., Marone, F., Van Swygenhoven, H., [2020] "Additive micro-manufacturing of crack-free PDCs by two-photon polymerization of a single, low-shrinkage preceramic resin," Additive Manufacturing 35, 101343.

Kulkarni, A., Sorarù, G.D., Pearce, J.M., [2020] "Polymer-derived SiOC replica of material extrusion-based 3-D printed plastics," Additive Manufacturing 32, 100988.

Kulkarni, A.D., Truhlar, D.G., Goverapet Srinivasan, S., Van Duin, A.C.T., Norman, P., Schwartzentruber, T.E., [2013] "Oxygen interactions with silica surfaces: Coupled cluster and density functional investigation and the development of a new ReaxFF potential," Journal of Physical Chemistry C 117, 258-269.
Larson, N.M., Zok, F.W., [2018] "In-situ 3D visualization of composite microstructure during polymer-to-ceramic conversion," Acta Materialia 144, 579-589.
Li, Y.J., Fan, C.Y., Zhang, J.P., Wu, X.L., [2018] "A promising PMHS/PEO blend polymer electrolyte for all-solid-state lithium ion batteries," Dalton transactions 47, 14932-14937.
Lu, K., Erb, D., Liu, M., [2016] "Thermal stability and electrical conductivity of carbon-enriched silicon oxycarbide," Journal of Materials Chemistry C 4, 1829-1837.
Ma, B., Cao, Y., Gao, Y., Wang, Y., [2018] "Fabrication of a thin double-layer thermistor based on DVB-modified polymer-derived SiCN ceramics," Journal of Alloys and Compounds 732, 491-497.
Ma, C., Ji, T., Robertson, C.G., Rajeshbabu, R., Zhu, J., Dong, Y., [2017] "Molecular insight into the Mullins effect: irreversible disentanglement of polymer chains revealed by molecular dynamics simulations," Physical Chemistry Chemical Physics 19, 19468-19477.
Merkel, T.C., Bondar, V.I., Nagai, K., Freeman, B.D., Pinnau, I., [2000] "Gas sorption, diffusion, and permeation in poly (dimethylsiloxane)," Journal of Polymer Science Part B: Polymer Physics 38, 415-434.
Plimpton, S., [1995] "Fast parallel algorithms for short-range molecular dynamics," Journal of computational physics 117, 1-19.
Ponomarev, I., Van Duin, A.C.T., Kroll, P., [2019] "Reactive Force Field for Simulations of the Pyrolysis of Polysiloxanes into Silicon Oxycarbide Ceramics," Journal of Physical Chemistry C 123, 16804-16812.
Smirnova, N., Tsvetkova, L., Lebedev, B., Zavin, B., Kotov, V., [2007] "Thermodynamics of polymethylhydrosiloxane based on 1, 3, 5, 7-tetramethyl-1, 3, 5, 7-tetrahydrocyclotetrasiloxane," Journal of thermal analysis and calorimetry 89, 217-222.
Stabler, C., Reitz, A., Stein, P., Albert, B., Riedel, R., Ionescu, E., [2018] "Thermal properties of SiOC glasses and glass ceramics at elevated temperatures," Materials 11, 279.
Taheri, P., Bokka, A., Asgari, P., Jeon, J., Lang, J.C., Campostrini, R., Sorarù, G.D., Kroll, P., [2020] "Novel Sulfur-Containing Cross-Linking Agent for Si-Based Preceramic Polymers," Macromolecular Chemistry and Physics 221, 1-9.
Toma, L., Kleebe, H.-J., Müller, M.M., Janssen, E., Riedel, R., Melz, T., Hanselka, H., [2012] "Correlation Between Intrinsic Microstructure and Piezoresistivity in a SiOC Polymer-Derived Ceramic," Journal of the American Ceramic Society 95, 1056-1061.
Vozza, A., [2021] "Mechanical Properties and Spectral Vibrational Response of Si-O-C With and Without Graphene Toughening," University of Central Florida.
Vry, S., Roumanie, M., Laucournet, R., Bernard-Granger, G., [2020] "Transmission Electron Microscopy Investigations on a Polysiloxane Preceramic Polymer Pyrolyzed at High Temperature in Argon," Ceramics 3, 421-427.
Wilfert, J., Jansen, M., [2011] "Curing preceramic SiBNC polymers infusible by radical polymerization," Journal of Materials Chemistry 21, 13422-13428.
Zhang, Y., Li, W., Huang, J., Cao, M., Du, G., [2020] "Expanded graphite/paraffin/silicone rubber as high temperature form-stabilized phase change materials for thermal energy storage and thermal interface materials," Materials 13, 894.